Fatigue of 8630 cast steel in the presence of porosity

K. M. Sigl†, R. A. Hardin, R. I. Stephens and C. Beckermann*

Department of Mechanical and Industrial Engineering, The University of Iowa, Iowa City, IA 52242, USA

Fatigue and monotonic test specimens having porosity ranging from micro- to macroscopic levels were cast from 8630 steel. Monotonic and fatigue properties were obtained to determine the effect of porosity on the mechanical performance of the cast steel. Axial fatigue tests were conducted under fully reversed conditions in both strain and load control on specimens containing microporosity, and in load control for specimens containing macropores. Monotonic tests revealed that specimens containing microporosity had strength properties comparable to sound material, but with substantially reduced ductility (76% less reduction in area). At stress amplitudes of 126 MPa, microporosity specimens were found to have lives greater than 5 million cycles (run-out) whereas macroporosity specimens had fatigue lives in the 10^2–10^4 cycle range at the same stress level. Fatigue lives for macroporosity specimens were in a range from 10^4 to 10^6 cycles when tested at the lowest stress amplitude, 53 MPa. The measured specimen elastic modulus was found to vary with porosity volume. Specimens with higher measured modulus outperformed the lower modulus specimens. Fatigue lives of the cast steel specimens were calculated using conventional models of fatigue behaviour, the strain–life and linear elastic fracture mechanics (LEFM) approaches. Life calculations made using the strain–life approach gave good agreement with measurements for specimens having microporosity, but this approach gave non-conservative results for macroporosity. LEFM modelling gave non-conservative results for both micro- and macroporosity specimens. For specimens with macroporosity, the calculations are difficult because of the porosity's complex shape and large size relative to the specimen, and the inability to determine the specific macropores responsible for fatigue failure of the specimens which is necessary for direct model-measurement comparisons. IJCMR/514

 Manuscript received 27 January 2004; accepted 20 April 2004.

Keywords: Porosity; Cast steel; Fatigue; Strain-life; Fracture mechanics

Introduction

Porosity in steel castings is a central concern of foundries. It results if there is insufficient liquid metal to feed a casting section as molten steel contracts during solidification and dissolved gases come out of solution. All porosity can be detrimental to strength and fatigue life of cast components because the pores act as stress risers within the casting and cracks can nucleate at pores leading to fracture. Despite this, the quantitative impact of porosity on the fatigue behaviour of steel castings is not fully understood, and there is no well accepted method to predict the effect of porosity on casting performance. As a consequence, design engineers have little choice but to use overly large safety factors in many designs, resulting in over-designed, heavy and expensive castings leading to increased costs and lead time, while decreasing casting yield and productivity. Other important features of the metal, such as microstructure, grain size, segregation at grain boundaries, and inclusions influence the fatigue and fracture behaviour as well, and these effects compete with one another and porosity. However, the objective of the current work is to study the relative effects of only micro- and macroporosity on fatigue behaviour of cast steel, and investigate models to predict their effects.

Since there are no performance-based guidelines for design of cast components where the amount or location of porosity is considered, it is difficult to assess during the design stage whether a cast component will be produced at a high enough quality level to meet its performance requirements. Conversely, a casting might be designed and specified at too high a quality level resulting in an over-designed, over-priced part. Current criteria for the acceptance or rejection of steel castings, such as the ASTM standard casting radiographs,[1–3] define only the 'qualitative' amount of porosity allowed in a casting. These standards consider only the relative amount of radiographically detectable macroporosity present in the casting and not the location or the size of the porosity contained within the casting and its relationship to the design. Furthermore, the radiographic standards do not address microporosity which may be undetectable, but is known to have a detrimental effect on material properties. In the case of microporosity, the engineering approach investigated in this work is to predict the formation of microporosity during the casting process and, then, to design the part considering the impact of microporosity on performance using fatigue and/or fracture mechanics principles.

The size and location of porosity and the loading conditions have been shown to influence the fatigue strength and fatigue life of various castings with

†Present address: Lockheed Martin Aeronautics Company, P.O. Box 748, Fort Worth, TX 76101

*Corresponding author, email christoph-beckermann@uiowa.edu

 DOI 10.1179/136404604225020588

larger pores in the higher tensile stress fields resulting in shorter fatigue lives.[4–8] The primary methods to calculate fatigue lives of cast specimens containing porosity involve modelling pores as equivalent notches or cracks.[4,7,9–12] Modelling of pores as elliptical or semi-elliptical cracks is the most common technique, but modelling pores as three-dimensional ellipsoidal notches has also been evaluated.[9] Modelling pores as three-dimensional notches uses a local strain model to calculate the fatigue lives of components. The local strain model assumes that crack nucleation encompasses the majority of the life of the component. Linear elastic fracture mechanics, LEFM, is used to model pores as pre-existing cracks within the component, and assumes that crack propagation will consume the majority of the fatigue life.

In this investigation, the effects of porosity on the fatigue behaviour of axially loaded 8630 quenched and tempered cast steel specimen were obtained. Then typical methods were used to calculate the fatigue lives of the specimens. A recently developed porosity prediction algorithm was used to design and produce cast specimens having a wide range of porosity as shown in Fig. 1.[13] This algorithm has been implemented within the commercial casting simulation software MAGMAsoft as a software module.[14] This computational tool predicts the location, volume percentage and size of porosity in castings ranging from radiographically undetectable microporosity to macroporosity. Four casting geometries were designed with this software to produce specimens with three levels of radiographically detectable macroporosity (termed 'least', 'middle' and 'most'), and test specimens with only microporosity. Other than porosity level, the as cast specimen blanks were produced to reduce as much as possible their variability in microstructure and inclusion content by casting them from the same heat of metal, with all types of specimens together in the same mould box, and heat treating them all together. Fatigue testing in accordance with ASTM standards was then performed using 10 stress/strain amplitudes for 14 microporosity specimens, and four stress amplitudes for 25 macroporosity specimens. Fractography and microscopy were conducted on the fracture surfaces using a scanning electron microscope, SEM, upon completion of mechanical testing.

Microscopy work was conducted on fracture surfaces, and cut and polished sections, of the microporosity and macroporosity porosity specimens. Analysis was conducted on both the macro- and microscopic levels using microporosity specimens and specimens from each macroporosity porosity group to understand the fracture morphology and pore geometry. Regions of fatigue crack nucleation and growth were of particular interest and were studied to determine the actual cause of failure. Determination of the pore sizes, shapes, and locations responsible for specimen failure are required in fatigue life calculations. Microscopy was performed to obtain what could be considered average pore geometries and volumes from ground surfaces from within the gage sections of the specimen groups. This information combined with the crack nucleation data gathered from fractography was used to calculate specimen fatigue life. Calculated and experimental specimen fatigue lives were then compared.

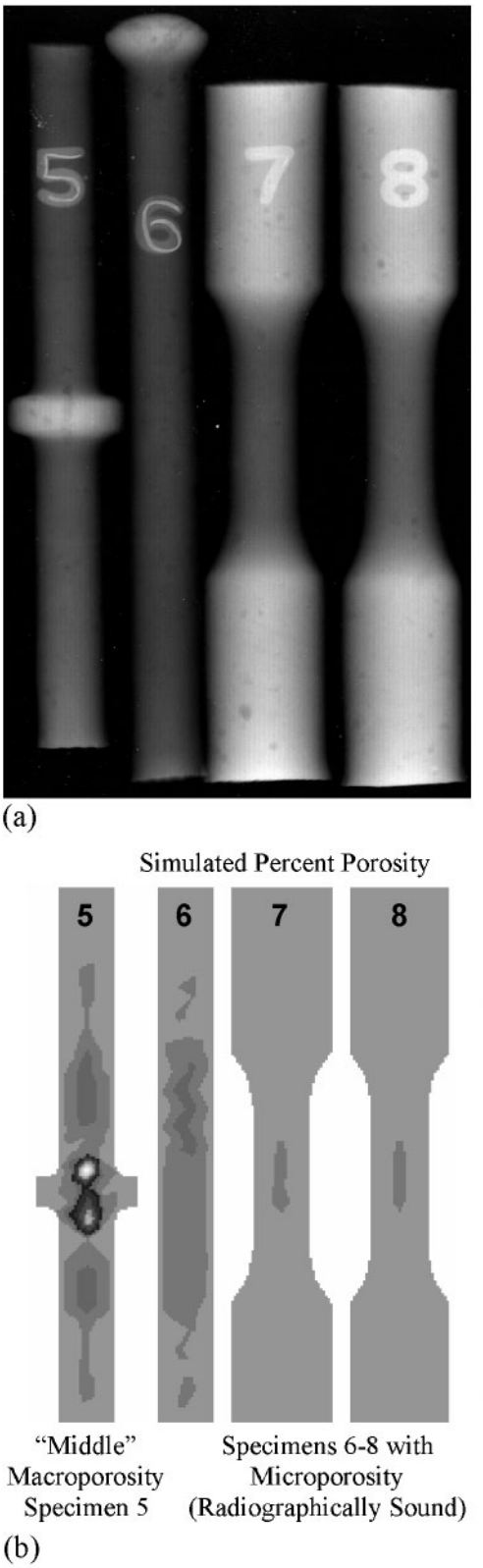

1 Typical comparison between *a* radiographs of specimen blanks and *b* computer model predictions of specimen blanks porosity volume percentages

Experimental procedure

Test specimens

Test specimens used in this investigation were prepared from AISI 8630 quenched and tempered

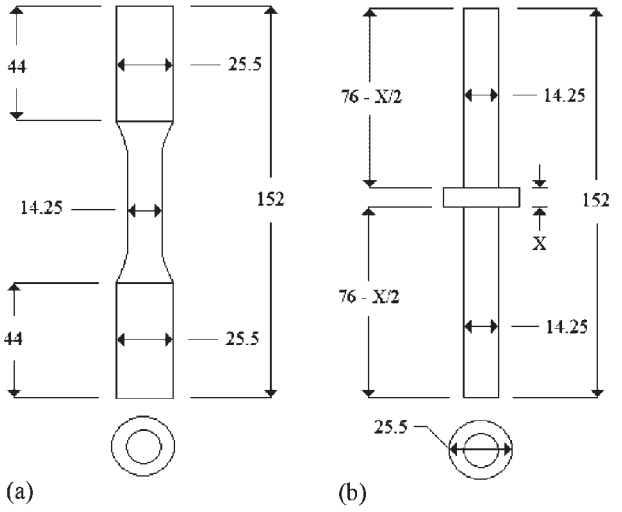

a microporosity specimen blanks; *b* macroporosity specimen blanks

2 Dimensions of cast blanks in millimetres. Dimension 'X' = 5, 7·5 and 10 mm for 'least', 'middle' and 'most' macroporosity specimen groups, respectively

cast steel. The composition (wt-%) was 0·93 Mn, 0·66 Si, 0·50 Ni, 0·48 Cr, 0·29 C, 0·27 Mo, 0·045 Al, 0·022 S and 0·027 P. Microporosity specimen blanks (Fig. 2*a*) were cast with reservoirs of molten steel at the ends of the blank with a narrow gage section located in the centre in an attempt to minimise the occurrence of macroshrinkage in the casting. Specimen blanks with macroporosity (Fig. 2*b*) were cast as 14 mm dia. cylinders with an approximate 25 mm dia. disc located at the mid-length of the casting to create a hot spot where the porosity would form. The amount of porosity in the casting was controlled by changing the thickness of the central disc, with more porosity occurring in the castings with thicker discs. Casting simulation (Fig. 1*b*) predicts a maximum porosity of approximately 0·5% in the gage section of the microporosity specimen blanks, and a porosity range between 2 and 25% in the macroporosity specimen blanks depending on the central disc thickness.

All cast blanks received identical heat treatment; normalised at 900°C, austenised at 885°C, water quenched, and finally tempered for 1·5 h at 510°C. This heat treatment resulted in a tempered martensitic structure with a Rockwell C hardness of 34. This heat treatment matched that used on the 8630 steel tested in a 1982 Steel Founders' Society of America (SFSA) study[15] to produce specimens having the same material properties as this baseline data. Specimens used in the 1982 SFSA report were machined from large cast trapezoidal-shaped keel blocks, and data from the report[15] will be referred to as 'sound' specimen data throughout the remainder of this paper. After heat treatment, each cast specimen blank was machined into a round test specimen with the final polished dimensions shown in Fig. 3. Machining followed the ASTM E606[16] standard that provides guidelines for specimen preparation, geometry, final surface finish and uniformity.

The machined specimens were examined through visual inspection and radiographic analysis to

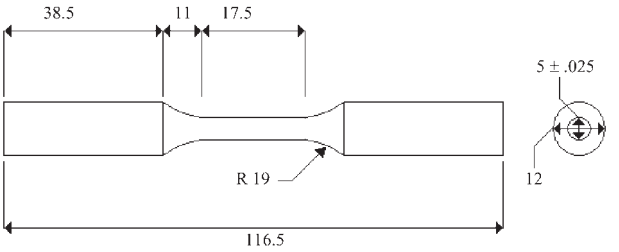

3 Final dimensions of fatigue specimens in millimetres

determine a qualitative measure of the porosity present in each casting group. Typical radiographs of selected specimens are shown in Fig. 4. Visual inspection showed that two of the 15 microporosity specimens and 27 of the 29 specimens with macroporosity had exposed pores at the specimen surface. No porosity was detectable in the radiographs of the microporosity specimens; they appeared to be radiographically sound. The micropores were too small (<200 μm diameter) to be detectable by the radiographic analysis used. Based on the radiographs of the macroporosity specimens, it was observed that the 'least' and 'middle' porosity groups contained very similar amounts of macroporosity with pore radii of approximately 0·75 mm. The 'most' porosity group of specimens showed the presence of even larger voids. In a study of the ASTM standard radiographs,[17] it was shown that the equivalent radii of the porosity in the radiographs (determined by two times the area of a radiographic indication divided by its circumference) were in a range from 0·6 to 1·1 mm over all five ASTM levels of porosity severity. For the three lowest levels of porosity in the ASTM standard radiographs (including all types, A, B and C), it was found that the average equivalent radius of porosity was approximately 0·75 mm,[17] which agrees well with

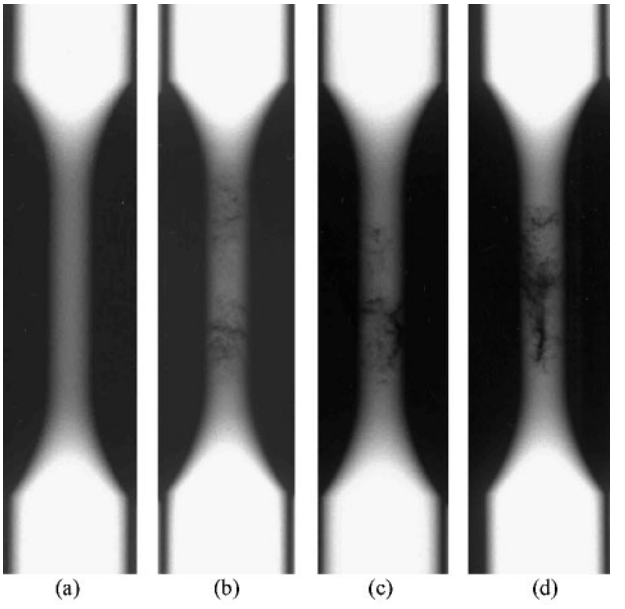

4 Radiograph images of *a* microporosity specimens, *b* 'least' macroporosity specimens, *c* 'middle' macroporosity specimens, and *d* 'most' macroporosity specimens

observations of the 'least' and 'middle' porosity groups examined here. It was concluded[17] that the typical size of macropores detected through the ASTM Standards[1–3] was about 0·75 mm with larger sizes forming in worse porosity through the merging of pores.

Mechanical testing

Testing was performed using a 100 kN closed loop servo-hydraulic test system. All fatigue tests were performed under fully reversed ($R=-1$) loading conditions. The alignment of the load frame gripping fixtures was verified according to ASTM Standard Practice E1012, Type A, Method 1, and meeting the requirements of ASTM E606, which requires that 'the maximum bending strains so determined should not exceed 5% of the minimum axial strain range imposed during any test program.'[16,18]

Monotonic and fatigue property data of the 8630 steel with microporosity were obtained first, before the macroporosity specimens. Monotonic tests were conducted in displacement control following standard ASTM E08 that provides guidelines on specimen preparation, geometry, surface finish, diameter measurement, test machine preparation, grips, alignment, rate of testing and determination of tensile properties.[19] Testing procedures for strain controlled low cycle fatigue (LCF) tests outlined in ASTM E606, that provides guidelines for alignment, calibration, grips, transducers, fixtures, cycle counting, extensometers, test environment, wave form, frequency, number of specimens and failure criteria, were followed to gather the needed cyclic and fatigue properties.[16] Tests conducted in strain control had constant strain rates of 0·01 s^{-1} with frequencies varying between 0·25 and 1·25 Hz. At smaller strain amplitudes, the behaviour of the specimens was predominantly elastic, making it possible to approximate strain amplitudes using load control. Cycling specimens in load control allowed the testing speed to be increased to 10–30 Hz with lower frequencies used for higher stress amplitudes.

All 'least', 'middle' and 'most' macroporosity specimens were run in load control at 10–20 Hz. The extensometer was also used on these tests to produce readings for the elastic modulus E. These data were collected to determine whether a relationship between the apparent elastic modulus and the porosity volume measured from the radiographs could be established. Specimens with macroporosity were tested at four different stress levels with the first stress level chosen as 126 MPa; note this was the run-out stress amplitude for the specimens with microporosity. The second stress level of 66 MPa was chosen by converting the strain–life ε–N curve of the microporosity specimens to a stress–life, S–N, curve and then shifting this curve down to the lives of the specimens with macroporosity previously tested. This adjusted S–N curve was then used to estimate stress amplitude and lives of the specimens with macroporosity. The goal was to obtain a life on the order of 10^6 cycles without a run-out occurring. The remaining stress levels were chosen to fill in gaps within the macroporosity specimen data. All fatigue tests were performed until fracture of the specimen occurred, or a run-out life was achieved at 5×10^6 cycles.

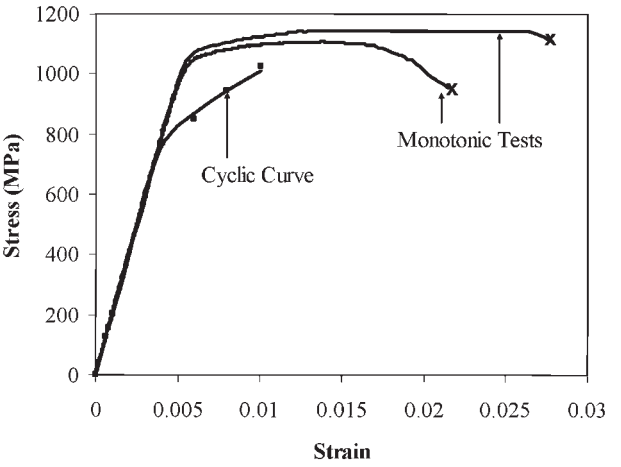

5 Monotonic and cyclic stress–strain curves of microporosity specimens

Experimental results

Monotonic testing

Monotonic material tensile properties were obtained from two microporosity specimens with the average results shown in Table 1. In this table, the ultimate tensile strength, S_u, yield strength, S_y, Young's Modulus E, per cent reduction of area, %RA, per cent elongation, %EL, true fracture strength σ_f, true fracture ductility ε_f, strength coefficient K and strain hardening exponent n are given for the microporosity specimens. Only values for S_u, S_y, E, %RA, σ_f and ε_f may be compared to the sound specimen data,[15] since %EL, K and n were not given in the earlier study. Monotonic tensile stress–strain curves for the specimens with microporosity are shown in Fig. 5. As is evident in Table 1, both the sound and microporosity material gave similar properties for E, S_u and S_y, found by the 0·2% offset method. The %RA for the microporosity specimens was found to be 76% lower than the %RA for the sound specimens. Neither monotonic microporosity test specimen showed signs of necking, and, in conjunction with small values of %RA and %EL, these tests indicate that the specimens with microporosity exhibited low ductility.

Table 1 8630 steel monotonic properties

Property	Micropore material avg.	Sound material[15]
S_u, MPa	1125	1144
S_y, MPa	1088	985
E, GPa	197	207
%EL	2·5	–
%RA	7·0	29
σ_f, MPa	1156	1268
ε_f	0·073	0·35
K, MPa	1307*	–
n	0·0279*	–

*Not the arithmetic mean but the best fit regression to the aggregate data.

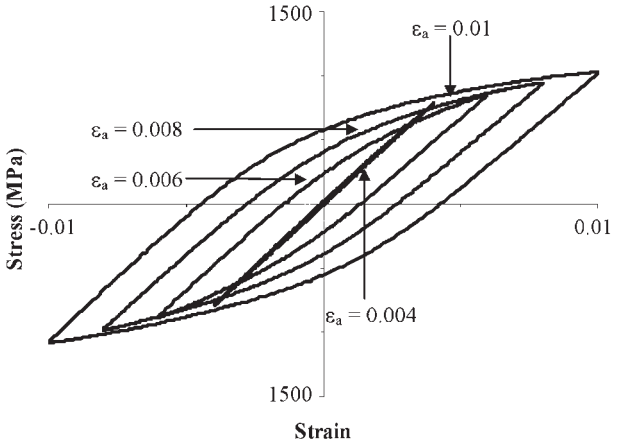

6 Halflife hysteresis loops used to create cyclic stress–strain curve for microporosity specimens

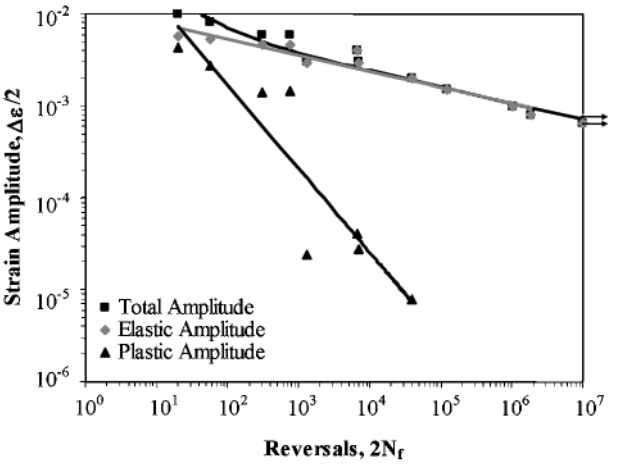

7 Total, elastic and plastic strain–life curves of microporosity specimens

Microporosity specimen fatigue testing

Cyclic and fatigue material properties for the microporosity specimens are shown Table 2, and they are again compared with the results for the sound specimens.[15] The first two entries in Table 2 are the fatigue strength (or fatigue limit) S_f at 5×10^6 cycles, and the fatigue ratio S_f/S_u. The fatigue ratio is reduced by more than a factor of 2 from the sound data. Via the 'companion' sample method, the cyclic stress–strain curve shown in Fig. 5 was generated using the approximate halflife stable hysteresis loops from a series of fatigue tests run at six strain amplitudes ε_a. In this process, the tensile points (loop tips) of the stabilised hysteresis loops at the specimen halflife are connected as shown in Fig. 6 to form the curve. In Fig. 6, only four of the six strain amplitudes tested are discernible; the lowest two strain amplitudes collapse onto the curve for $\varepsilon_a = 0{\cdot}004$. The cyclic stress–strain curve is used to determine the material properties which relate the nominal true stress and true strain ranges as given by equation (1)

$$\Delta e = \frac{\Delta S}{E} + 2\left(\frac{\Delta S}{2K'}\right)^{\frac{1}{n'}} \quad . \quad . \quad . \quad . \quad . \quad . \quad . \quad . \quad . \quad (1)$$

where the symbols ΔS and Δe are the nominal true axial stress and true axial strain, respectively, E is Young's modulus, K' is the cyclic strength coefficient, and n' is the cyclic strain hardening exponent. Values of these parameters are given in Table 2 for the sound and microporosity material. The value of cyclic yield strength S_y' was found to be 894 MPa, which is less than S_y (comparing Tables 1 and 2), indicating that the material cyclic softened. Cyclic softening commonly occurs with high strength materials and results in softening of the material as the cyclic loading progresses. The majority of softening occurred within the first 10–20% of specimen life, and then slowed to an approximate constant slope of decreasing maximum stress in tension, and increasing minimum stress in compression.

Table 2 8630 steel cyclic properties

Property	Micropore material	Sound material[15]
S_f, MPa	126	293
S_f/S_u	0·11	0·26
K', MPa	2550*	1502/2267†
n'	0·167*	0·122/0·195†
S_y', MPa	894*	682/661†
b	−0·176	−0·121
c	−0·908	−0·693
σ_f', MPa	2390	1936
ε_f'	0·11	0·42

*Data determined from the companion method.
†Data determined from the companion and incremental step methods, respectively.

A strain versus reversals to failure ε–$2N_f$ curve (Fig. 7) was constructed from the plastic and elastic curves, which when summed produce the total ε–$2N_f$ curve equation

$$\frac{\Delta\varepsilon}{2} = \frac{\Delta\varepsilon_e}{2} + \frac{\Delta\varepsilon_p}{2} = \frac{\sigma_f'}{E}(2N_f)^b + \varepsilon_f'(2N_f)^c \quad . \quad . \quad . \quad (2)$$

where $\Delta\varepsilon/2$ is the total strain amplitude, $\Delta\varepsilon_e/2$ is the elastic strain amplitude, $\Delta\varepsilon_p/2$ is the plastic strain amplitude, σ_f' is the fatigue strength coefficient, b is the fatigue strength exponent, ε_f' is the fatigue ductility coefficient, and c is the fatigue ductility exponent. The values for σ_f', b, ε_f' and c from the microporosity specimens are given in Table 2 and were determined by a curve fit of the test data. Comparison between the microporosity and sound data in Table 2 reveals the largest difference to be the fatigue ductility coefficient. In equation (2), the first addition term is the equation of the elastic strain amplitude curve, and the second term is the equation of the plastic strain amplitude curve. Many steels behave in a predominantly plastic manner under high strain amplitudes, and in a predominantly elastic manner at lower strain amplitudes with a transition point where the elastic and plastic curves cross. It was observed that this transition point never occurred in the microporosity specimens as the elastic strain amplitudes were always larger than the plastic strain amplitudes. At strain amplitudes of 0·004 and below, plastic strains were virtually nonexistent, and the $\Delta\varepsilon_e/2$ data points can be seen to fall directly on top of the $\Delta\varepsilon/2$ data points.

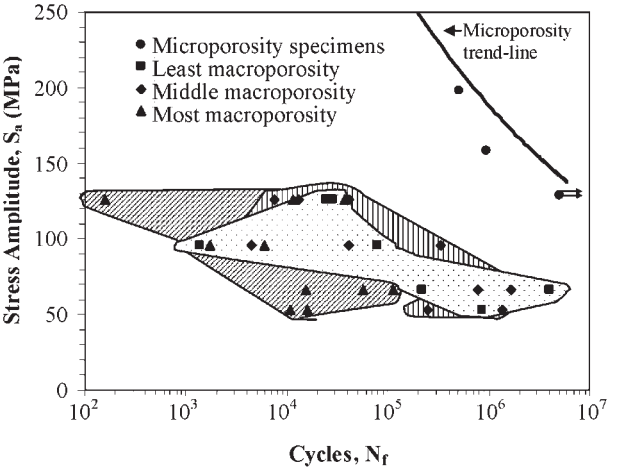

8 Porous material fatigue data with scatterbands; dotted pattern, 'least' porosity; vertical shading, 'middle' porosity; inclined shading, 'most' porosity

Macroporosity specimen fatigue testing

The fatigue test conditions and test results for all specimens with macroporosity are given in Table 3. They are grouped by 'least', 'middle' and 'most' porosity specimen geometry types, and then from largest to smallest stress amplitude level within each group. Experimental fatigue results of the 'least', 'middle', and 'most' macroporosity levels are shown in comparison to the microporosity specimens in the stress–life, *S–N*, curve of Fig. 8. Scatter bands are drawn around each of the three porosity groups. The scatterbands for the 'least' and 'middle' porosity groups show significant overlap, indicating that the groups had similar fatigue lives. The scatterband for the 'most' porosity group falls farther to the left of the 'least' and 'middle' porosity groups and has fewer areas of overlap, demonstrating generally lower experimental fatigue lives at the same stress level. Note that all of the macroporosity specimens had considerably shorter fatigue lives than the lives of the microporosity bearing material, and were tested below the microporosity specimens fatigue limit for the majority of the fatigue testing.

A modulus of elasticity E_{meas} of each macroporosity specimen was measured during testing to determine whether the porosity level and measured modulus could be correlated. It was also believed that this might serve as an indicator of porosity volume. This 'apparent' specimen modulus is reduced from the modulus of sound specimens by the lost section thickness associated with porosity. The modulus of the microporosity test specimens was only 5% lower than the sound data[15] as seen in Table 1, and this difference could be attributable to normal variability and/or the greater microporosity. As determined from the data in Table 3, the macroporosity specimen modulus values were 20–63% lower than the sound material modulus, and 16–61% less than the microporosity specimen measured modulus. Measured modulus ranges of 137–153, 111–166 and 77–136 GPa were found in the 'least', 'middle' and 'most' specimen groups, respectively. Note that the 'least' and 'middle' specimen groupings had mean E_{meas} of approximately 144 GPa and produced similar experimental fatigue results, and the mean measured modulus of the 'most' specimens was 113 GPa. Both the 'least' and 'middle' materials had a mean measured modulus significantly higher than the 'most' porous material and outperformed the 'most' porous specimens in fatigue testing.

Table 3 Macroporosity specimen load control test data and results

Specimen ID	Porosity level	Stress amp, MPa	N_f	*E*, GPa	Calculated stress, MPa
C4	Least	126	24 320	143	174
C8	Least	126	29 023	153	163
C2	Least	96	1365	137	138
C3	Least	96	79 908	149	127
C9	Least	66	216 516	145	90
C10	Least	66	4 053 800	141	92
C5	Least	53	851 275	138	76
H8	Middle	126	7456	148	168
G5	Middle	126	13 013	142	175
H3	Middle	126	40 896	155	161
G2	Middle	96	4392	111	171
G8	Middle	96	41 066	125	152
H7	Middle	96	333 025	142	134
H2	Middle	66	769 074	151	86
G1	Middle	66	1 681 018	166	79
G7	Middle	53	249 752	143	73
G4	Middle	53	1 342 218	145	72
E6	Most	126	160	120	207
E8	Most	126	11 648	136	183
D6	Most	126	37 089	135	184
E1	Most	96	1935	90	211
E5	Most	96	6042	77	246
D10	Most	66	15 419	113	115
D4	Most	66	57 566	135	97
D8	Most	66	113 503	136	96
D5	Most	53	10 812	87	120
E10	Most	53	15 868	104	101

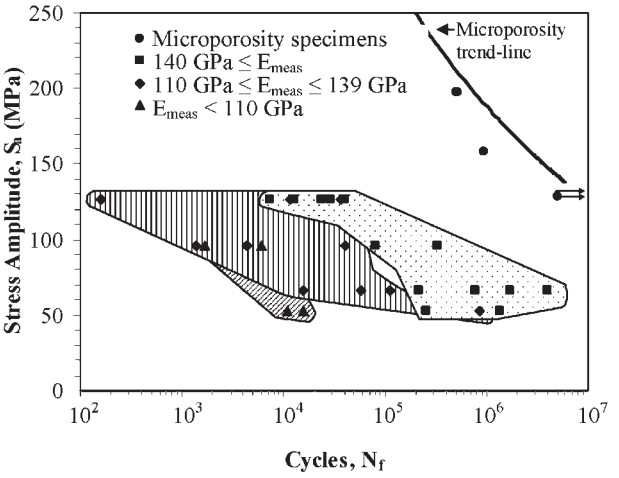

9 Porous material fatigue data grouped by modulus E_{meas} with scatterbands; dotted pattern, modulus 140 GPa and greater; vertical shading, modulus 110–139 GPa; inclined shading, modulus less than 110 GPa

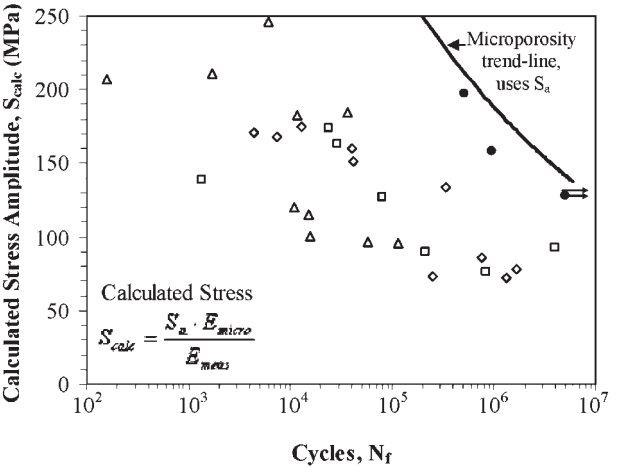

10 Calculated stress amplitude macroporosity data; squares, 'least' porosity; diamonds, 'middle' porosity; triangles, 'most' porosity; and test stress amplitude data S_a for (filled circles) microporosity material

Based on the relationship between the measured specimen modulus and fatigue life, a more appropriate grouping of specimens would be on the basis of measured modulus rather than specimen casting geometry. Therefore, new macroporosity groupings based on measured moduli of 140 GPa and greater, 110–139 GPa, and moduli less than 110 GPa were made, approximately splitting the total range of moduli data into thirds. These new groups are plotted in the S–N_f graph of Fig. 9 which has scatterbands drawn around the measured modulus groupings. Generally, the data when plotted in these three new groupings show that the higher modulus specimens outperformed the lower modulus specimens, and that categorising the data based on measured modulus provides a better grouping, with less overlap, than the as cast geometry did in Fig. 8.

All macroporosity tests were conducted using load control. This meant that the amplitude of the axial force on the specimen was determined based on the nominal specimen cross-sectional area and the desired stress amplitude levels before testing. The nominal specimen area was determined from diameter measurements made using an optical microscope without consideration of porosity. This test amplitude stress is lower than the true stresses experienced by the specimen material since the specimen area is reduced by the macroporosity. Assuming that the decrease in measured modulus is because of the reduced volume caused by porosity, there is a reduction in the effective cross-sectional area of the specimen test section. Considering this, a better representative value of the 'effective' stress amplitude applied to the macroporosity test specimens is calculated by equation (3)

$$S_{calc} = \frac{S_a \cdot E_{micro}}{E_{meas}} \quad \ldots\ldots\ldots\ldots (3)$$

where E_{micro} and E_{meas} represent the modulus of the microporosity specimens and macroporosity test specimens, respectively, and S_{calc} and S_a represent the newly calculated 'nominal' applied stress amplitude, and the original stress amplitude based on a sound test specimen, respectively. Using this equation, the calculated test stress amplitudes ranged from approximately 70 to 250 MPa instead of the four stress amplitude groups of 53, 66, 96 and 126 MPa. The calculated stress is given in Table 3 for each test specimen. New data points using the calculated stresses, shown as open shapes, are shown in the S–N_f plot in Fig. 10. From Fig. 10, the test specimens fall into a power function pattern with the higher stresses generally seeing shorter lives than the lower stresses, as is normally expected with fatigue data. Even with the calculated nominal stress, the specimens with macroporosity still had significantly shorter lives than the microporosity specimens with similar stress amplitudes. It is apparent that using this representative stress amplitude alone does not entirely explain the poor fatigue behaviour of the specimens with macroporosity. The actual stresses responsible for failure are even higher than these calculated stresses. The calculated stresses in Fig. 10 are based on a measured modulus arising from the entire specimen test section and are not determined at the failure initiation sites.

Results of the fatigue testing of the micro- and macroporosity specimens are compared with the sound material test curve[15] in Fig. 11. Note that the microporosity data (dashed curve) depart more from the sound data (solid curve) at decreasing levels of stress, and at lower levels of stress (300 MPa), the fatigue life is reduced by a factor of about 100. Since this microporosity is difficult to detect, it may point to a cause of the overly large safety factor applied by designers to cast material throughout an entire cast part in lieu of the ability to predict the presence of microporosity in parts and design for its localised effects. The ratio of the stress amplitudes of the microporosity specimens to macroporosity specimens range from 5 at 10^2 cycles to failure to 3 at 10^5 cycles, which emphasises the dramatically reduced fatigue resistance associated with macroporosity. Run-out tests ($N_f > 5 \times 10^6$ cycles) occurred at the 126 MPa stress level in the microporosity test specimens.

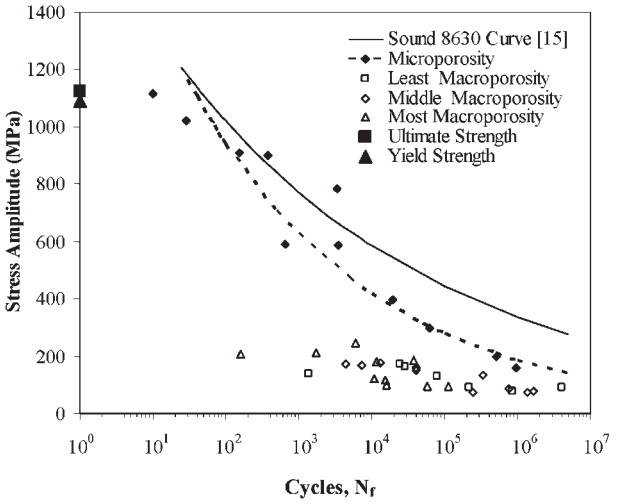

11 Stress amplitude versus cycles to failure for sound cast 8630 material property curve,[15] microporosity data and macroporosity data using calculated stress amplitude from equation (3)

The results of the fatigue testing point to the importance of integrating the prediction of porosity in the casting process with the casting design. In the case of microporosity, since it is difficult to detect using nondestructive inspection (NDI), predicting microporosity in the casting process and considering its effect on fatigue life of the part will be useful in designing and producing parts with greater durability and reducing overly large factors of safety applied to design calculations. The results for the macroporosity specimens provide a lower bound or worst case boundary for property. Certainly more research into the effects of macroporosity and an explanation for the significant data scatter observed here are warranted. Unless an engineering approach can be developed to conservatively consider the effects of macroporosity on the casting performance, good casting practices and NDI must be relied upon to prevent it from occurring.

Fractography and microscopy

Specimens with microporosity

Following the axial testing, the specimen fracture surfaces were examined with the use of a scanning electron microscope (SEM). The examination revealed two types of cyclic failures for the microporosity specimens. Specimens tested at strain amplitudes greater than or equal to $\varepsilon_a = 0{\cdot}003$ showed essentially no fatigue regions and had very rough and jagged fracture surfaces. These are similar to the monotonic fracture surfaces, which despite the low values of per cent elongation and per cent reduction in area, were widely covered with ductile dimples as shown in Fig. 12. Ductile dimples are formed at discontinuities such as second-phase particles, inclusions, or grain boundaries within the steel and begin to grow and coalesce into cracks that eventually lead to fracture of the component.[20] This microvoid coalescence is typically associated with ductile fracture.

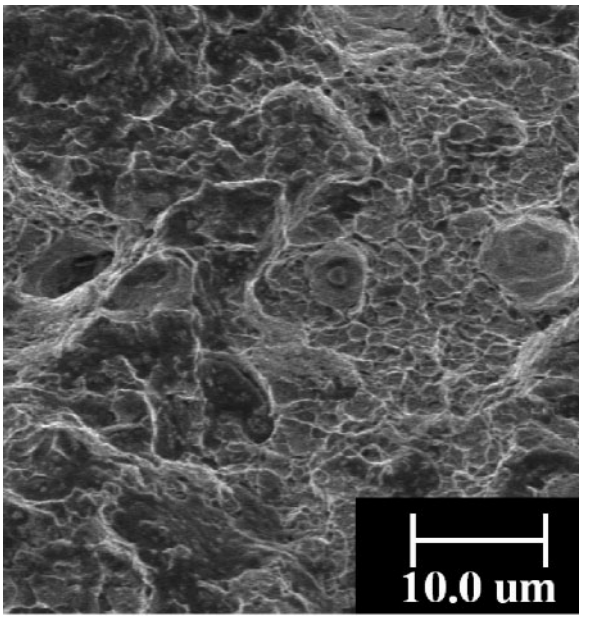

12 Typical ductile dimples found in final fracture regions of microporosity specimens

Specimens tested at strain amplitudes below $\varepsilon_a = 0{\cdot}003$ had flat regions in the fracture surface indicating areas of fatigue crack growth (FCG). Clear regions of crack nucleation and final fracture were also observed in these specimens. The final fracture region was composed primarily of ductile dimples (Fig. 12) and the FCG region was composed of fatigue facets. Typical fatigue facets found in the FCG region are shown in Fig. 13. Three low strain amplitude specimens were evaluated under the SEM, and all were found to have cracks that nucleated from surface or near-surface porosity approximately 200 μm in diameter such as shown in Fig. 14.

No indication of unsoundness was observed on the radiographs for all microporosity specimens. Three of the 15 microporosity specimens were examined under 20–3000 × magnification. Pores of 100–200 μm dia.

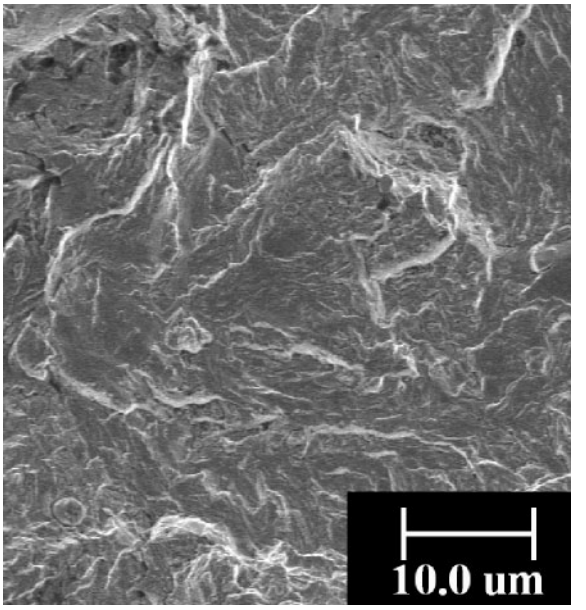

13 Typical fatigue facets found in FCG regions

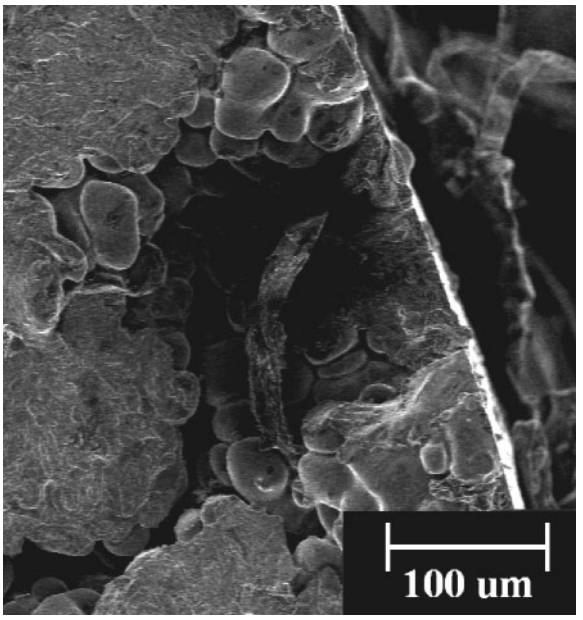

14 Near surface micropore of approximately 200 μm diameter

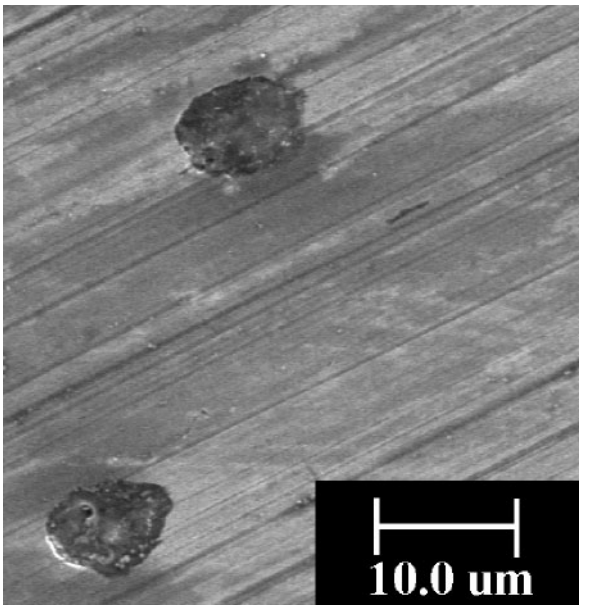

15 Typical micropores found on ground surface

were observed in the fracture surface of these three specimens. Only after sectioning the microporosity specimens approximately 5 mm behind the fracture surface, and polishing to a mirror surface finish, was the widespread presence of micropores revealed. The observed micropores on the polished surface were nearly spherical in shape with diameters ranging from approximately 2–20 μm. Larger pores on the order of 200 μm, as found in three specimens on the fracture surface, were not evident in any ground and polished sections. On the polished surfaces, the micropores were not distributed evenly across the surface; therefore, a conservative estimate of total local micropore volume gathered by measuring the total micropore surface area from a high micropore concentration region is approximately 0·65%. An image of typical micropores found on the ground surface is shown in Fig. 15.

Specimens with macroporosity

Eight specimens with macroporosity were chosen to have their fracture surfaces examined with the SEM. The fracture surfaces fell into two categories: those that showed clear evidence of fatigue fractures such as in Fig. 16*a*, and those that did not (Fig. 17*a*). Specimens with evidence of fatigue fractures typically had a FCG region as indicated by a large flat region on a macroscopic view, and had the appearance of fatigue facets on a microscopic view. In several specimens, a final fracture region was found on the macroscopic level as a shiny region containing a small but identifiable shear lip. Upon evaluation of the final fracture region on a microscopic level, ductile

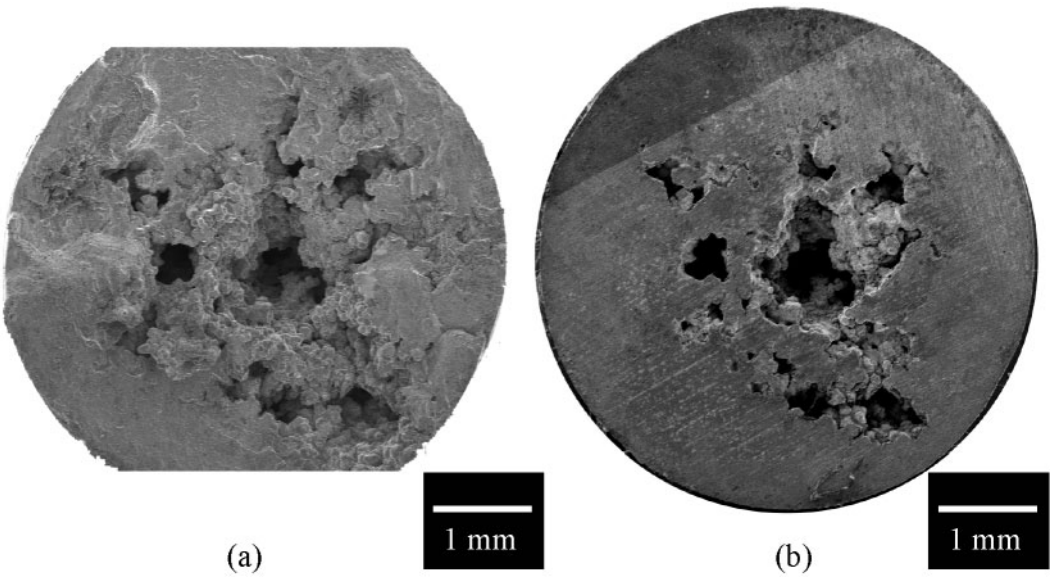

16 Macroporosity specimen; *a* fracture surface showing signs of FCG near edges of specimen and *b* ground surface

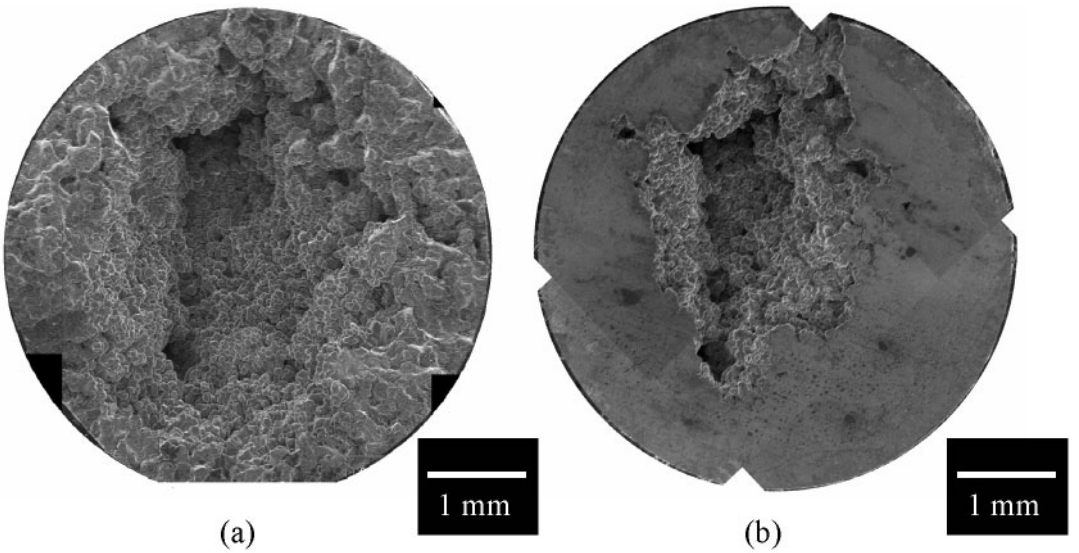

17 Macroporosity specimen; *a* fracture surface with no signs of macroscopic fatigue and *b* ground surface

dimpling was observed as was the case with the microporosity specimens. Unfortunately, none of the specimens showed a clearly identifiable region of crack nucleation at a specific pore. This introduces uncertainty to the application of predictive fatigue life models.

Fracture surfaces of the eight specimens selected for study were ground back to more clearly show the porosity present within the specimen. The polished surfaces of the specimens are shown aligned in the same orientation as the fracture surfaces in Figs. 16*b* and 17*b*. The total macropore surface areas of the polished surfaces were then measured using image analysis, dividing this by the total cross-sectional area of the specimens gives porosity ranging from approximately 2·2 to 30·9% for the eight specimens. Also a 'calculated' porosity percentage was determined from the measured elastic modulus E_{meas} of each specimen according to equation (4)

$$\text{Calculated porosity } \% = 100\left(1 - \frac{E_{meas}}{E_{micro}}\right) \qquad (4)$$

where the constant E_{micro} is the modulus of the specimens with microporosity. The measured pore area percentages are compared to calculated porosity percentages in the third and fourth columns of Table 4. It should be noted that the macroporosity was not uniformly spread throughout the gage section of the specimens. Therefore the measured pore area percentages are not entirely representative of the pore volume of these specimens and are merely a snapshot of a section near the region of fracture. Though their magnitudes are different, the calculated and measured porosities appear to be in somewhat relative agreement between specimens.

Modelling microporosity in fatigue life calculations

Fatigue life calculations for microporosity by strain–life approach

The fatigue lives of the specimens with microporosity were calculated using the strain–life approach and modelling the micropores as notches. The pores responsible for crack nucleation in the three specimens examined were spherical-shaped with a diameter of approximately 200 μm. This pore size is small compared to the 5 mm dia. of the specimen at the gage section. Therefore, the micropores were modelled as a spherical notch contained within an infinite body, giving a stress concentration factor K_t equal to 2·05.[21] This K_t value was then increased by 7%, according to Eubanks,[22] to account for the vicinity of the crack nucleation pores near the surface of the specimens. The final value of K_t was thus taken to be 2·19.

The stress concentration factor was used to calculate a fatigue notch factor K_f. Fatigue strength

Table 4 Measured macropore and 3-D notch geometries

				Ellipsoidal notch information				
Specimen	Young's Modulus, *E*, GPa	Calc. porosity, %	Meas. pore area, %	3-D notch type	Major axis, 2a, mm	Minor axis, 2b, mm	K_t	K_f
H2	151	23·4	14·9	Neuber	2·25	1·8	2·36	2·23
G7	143	27·4	2·2	SS	2·01	0·43	2·82	1·70
C4	143	27·4	10·5	SS	1·50	0·75	2·47	2·05
C10	141	28·4	13·5	Neuber	1·75	1·00	2·97	2·56
C2	137	30·5	23·2	SS	3·33	1·15	2·66	2·21
E6	120	39·1	27·6	Neuber	2·35	2·00	2·27	2·17
E1	90	54·3	29·7	SS	4·10	1·79	2·54	2·30
D5	87	55·8	30·9	SS	4·00	2·35	2·37	2·24

depends not only on the stress concentration factor, but also on the notch radius, material strength, and mean and alternating stresses.[23] K_f was determined from K_t using[21,24]

$$K_f = 1 + \frac{K_t - 1}{1 + \alpha/r} \quad . \quad . \quad . \quad . \quad . \quad . \quad . \quad . \quad . \quad . \quad (5)$$

$$\alpha = 0{\cdot}0254 \cdot \left(\frac{2070}{S_u}\right)^{1{\cdot}8} \quad . \quad . \quad . \quad . \quad . \quad . \quad . \quad . \quad . \quad . \quad (6)$$

where, r is the notch root radius in millimetres, S_u is the ultimate tensile strength of the material in MPa, and α is a material constant in mm. It should be noted that equation (6) was originally developed for wrought steels.[24] Extending equation (6) to cast steels was the best approximation available for the constant α.

Nominal stresses were calculated at each strain amplitude tested, assuming perfectly sound specimens. This was accomplished using equation (1), which relates the nominal true stress ΔS and true strain ranges Δe. The local notch root stress and strain ranges were then calculated from the nominal stress and strain ranges by simultaneously solving Neuber's rule, equation (7), and the stable cycle hysteresis loop equation, equation (8), given below as

$$\Delta\varepsilon \cdot \Delta\sigma = K_f^2 \Delta e \cdot \Delta S \quad . \quad . \quad . \quad . \quad . \quad . \quad . \quad . \quad . \quad . \quad (7)$$

$$\Delta\varepsilon = \frac{\Delta\sigma}{E} + 2\left(\frac{\Delta\sigma}{2K'}\right)^{\frac{1}{n}} \quad . \quad . \quad . \quad . \quad . \quad . \quad . \quad . \quad . \quad . \quad (8)$$

where $\Delta\sigma$ and $\Delta\varepsilon$ are the local axial stress and strain at the notch root, respectively. The material properties, E, K' and n', were taken as those of the sound 'keel block' material as provided in Table 2.[15] The local notch strain range from equations (7) and (8) was then put into equation (2) to calculate the fatigue life of the specimens with microporosity.

Spheroid notches of 10, 20, 100 and 200 μm dia. were chosen to represent the range of possible pore sizes where the fatigue failure initiates. These representative values were chosen based on observations made on the fracture and polished surfaces, and demonstrate how micropore size data might be used to determine the effect of microporosity on the steel fatigue resistance. The resulting life calculations are shown in Table 5 and in graphical form in Fig. 18, which plots the strain amplitude ε_a versus cycles to failure N_f. Note that calculated run-out points are not indicated in Fig. 18, and note that life calculation modelling lines are extended out to 1×10^7 cycles. Any notched fatigue life values that are calculated to be greater than 5×10^6 cycles should be considered 'calculated' run-outs.

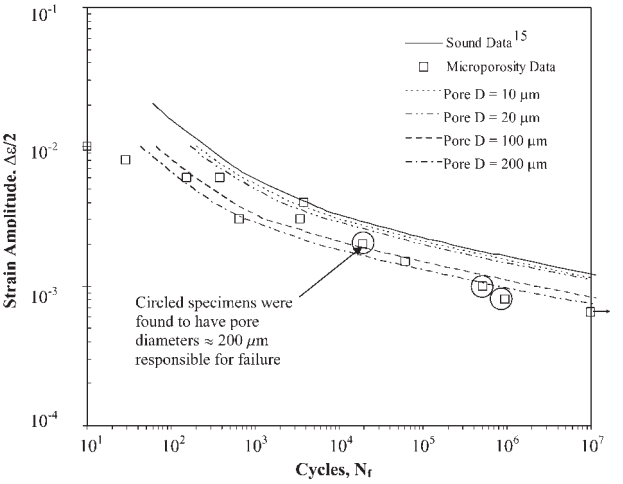

18 Local strain–life curve for sound material, microporosity data and model calculations for microporosity specimens using 10, 20, 100 and 200 μm dia. surface notches

The results shown in Fig. 18 are encouraging, since micropores responsible for the failure of the three circled specimens in Fig. 18 were observed to be nearly spherical in shape with diameters of approximately 100–200 μm and were located at, or near, the specimen surface. The three experimental data points agree better with the 100–200 μm pore size calculations than with the 10–20 μm pore or sound material curves. Calculations using micropores of 100–200 μm dia. result in reasonably accurate and conservative life calculations using the strain–life approach for all microporosity specimens. Also, the two run-out specimens that were tested at the lowest strain amplitude agree with the run-out calculation for the 200 μm sized pore. Examination of the micropore specimen fracture surfaces with a SEM showed that the specimens tested at high strain amplitudes, $\Delta\varepsilon/2 \geqslant 0{\cdot}003$, showed no clear indication of crack

Table 5 Comparison of experimental microporosity specimen fatigue lives and calculated fatigue lives for 200 μm spherical notch using local strain–life model

ε_a	Experimental N_f, cycles	Calculated N_f (cycles) for a 200 μm notch
0·01	10	27
0·008	29	40
0·006	153 and 381	70
0·004	3800	170
0·003	650 and 3476	300
0·002	19 299	2100
0·0015*	62 112	11 800
0·001*	517 015 and 512 858	222 000
0·0008*	951 965	1 240 000
0·00065*	Run-out†/run-out	Run-out

Note: fatigue lives for runs at repeated strain levels are separated by 'and'.
*Strain amplitude approximated using load control.
†Run-out was taken as 5 000 000 cycles.

nucleation, FCG, or final fracture regions whereas the specimens tested at low strain amplitudes, $\Delta\varepsilon/2 < 0{\cdot}003$, clearly demonstrated all of these features. This may explain the disagreement with the two points at the far left in Fig. 18. Since the most useful region of this figure is the high cycle range, these high strain levels would not be desirable in a design or application.

Modelling micropores by linear elastic fracture mechanics (LEFM)

Linear elastic fracture mechanics (LEFM) principles were used to calculate the microporosity specimen lives and compare with fatigue testing results. It is assumed that for the microporosity material, a fatigue crack of size 'a' has a crack growth rate of da/dN that can be modelled by the Paris equation

$$\frac{da}{dN} = A(\Delta K)^n \quad . \quad . \quad . \quad . \quad . \quad . \quad . \quad . \quad . \quad . \quad . \quad (9)$$

where A and n are material constants and ΔK is the mode I stress intensity factor range operating on the crack. The constants A and n are determined from crack test data for a given material, and unfortunately it was not feasible to measure fatigue crack growth properties in the current series of material testing for the microporosity specimens. Therefore, properties from the sound material, as given in Table 6,[15] were used in the LEFM calculations presented here.

For fully reversed testing, the value of ΔK was calculated using equation (10)

$$\Delta K = S_{max}\sqrt{\pi a}F \quad . \quad . \quad . \quad . \quad . \quad . \quad . \quad . \quad . \quad . \quad . \quad (10)$$

where S_{max} is the maximum stress, a is the crack depth, and F represents a shape factor that relates the geometry of the crack front to the crack depth. Equation (10) only takes into account S_{max} because the minimum stress intensity factor is undefined in compression and will have a value of zero. Additional crack closure was not incorporated. Substituting equation (10) into equation (9) and integrating from the initial crack depth a_i to the final crack depth a_f results in equation (11), giving the total cycles to failure.

$$N_f = \int_0^{N_f} dN = \int_{a_i}^{a_f} \frac{da}{A(S_{max}\sqrt{\pi a}F)^n} \quad . \quad . \quad . \quad . \quad . \quad (11)$$

Cracks responsible for the failure of the specimens were formed from pores located near or at the surface of the round specimens. Therefore, the cracks were modelled as semi-circular surface cracks. Forman created a model for semi-circular cracks growing in round bars, much like the cracks growing in these specimens.[25] Using this model, where D_{sp} is the diameter of the round specimen, the shape factor $F(a/D_{sp})$ becomes

$$F\left(\frac{a}{D_{sp}}\right) = g\left(\frac{a}{D_{sp}}\right)\left[0{\cdot}725 + 2{\cdot}02\,\frac{a}{D_{sp}} + 0{\cdot}37\left(1 - \sin\left(\frac{\pi}{2}\,\frac{a}{D_{sp}}\right)\right)^3\right] \quad (12)$$

$$g\left(\frac{a}{D_{sp}}\right) = 0{\cdot}92\left(\frac{2}{\pi}\right)\left[\tan\left(\frac{\pi}{2}\,\frac{a}{D_{sp}}\right)\Big/\left(\frac{\pi}{2}\,\frac{a}{D_{sp}}\right)\right]^{1/2}\Big/ \cos\left(\frac{\pi}{2}\,\frac{a}{D_{sp}}\right) \quad (13)$$

The initial crack length was taken as the square root of the projected area of the pore that nucleated the crack.[10,12] For simplicity, it was assumed that for all microporosity specimens, the cracks leading to fracture nucleated from 200 μm dia. pores. Therefore, an initial crack length of 177 μm was used for all micropore specimens. This assumed initial crack length is termed 'physically small' by ASTM Standard E647, since it is less than 1 mm.[26] Five of the eight stress levels resulted in ΔK below the long crack threshold stress intensity factor ΔK_{th} so small crack growth behaviour was assumed to exist. Since small crack growth behaviour was not evaluated for the sound specimens, this growth was calculated by extrapolating equations (9) and (11) into the small crack growth region from the sound data.[15] The specimens tested at strain amplitudes greater than $\varepsilon_a = 0{\cdot}0015$ were run in strain control, so the stable cycle stress taken from mid-life of the specimen was used as an approximation of S_{max}. The maximum stress used during testing must be less than or equal to eight-tenths of the yield strength for LEFM to be applicable. Therefore, two of the testing levels, $\varepsilon_a = 0{\cdot}01$ and $\varepsilon_a = 0{\cdot}008$, could not be evaluated with this procedure since the stable cycle tensile peaks were too large and violated LEFM restrictions.

The final crack length of each specimen was determined either at the point where net section yielding would occur, or at the point where the critical stress intensity factor K_c was reached. Some difficulty arises applying this method for final crack size determination in the Forman crack front model. The Forman model is only capable of reaching crack sizes equivalent to the radius of the specimen, as is demonstrated by the following equation for determining the crack length

$$r = \frac{a(2{\cdot}R_{sp} - a)}{2(R_{sp} - a)} \quad . \quad . \quad . \quad . \quad . \quad . \quad . \quad . \quad . \quad . \quad (14)$$

where r is the radius of the circle describing the crack front, a is the crack length, and R_{sp} is the specimen radius. As the crack length a approaches R_{sp}, the equation becomes undefined. If net section yielding could only be reached when a crack length larger than R_{sp} was reached, the crack shape was assumed to become a straight front, so net section yielding, and consequently a_f could be calculated. Equations (12) and (13) were used to calculate the stress intensity factor. It was found that all failures occurred by net section yielding.

Table 6 Crack growth properties

Property	Data used for calculations
S_y, MPa	1088
ΔK_{th}, MPa m$^{1/2}$	9·4*
K_c, MPa m$^{1/2}$	135
A, m cycle^{-1}	$2{\cdot}63 \times 10^{-12}$*
n	3·03*

*Properties from sound material[15] at $R = 0$.

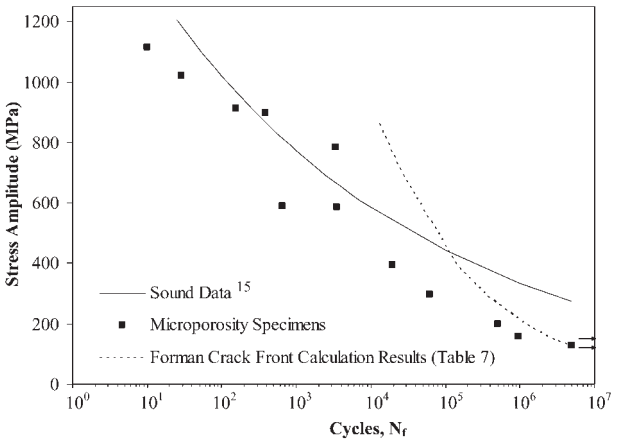

19 LEFM model calculations for microporosity specimens using crack length based on 200 μm pore compared with sound material and microporosity data

Table 7 gives specimen test information, and the experimental and calculated fatigue lives using the Forman crack front model. These results are compared in Fig. 19. It can be seen that LEFM calculations (dotted line) modelling the micropores as cracks overestimates life compared to all test data except the three longest life specimens. In the calculations, five of the eight strain amplitudes were not large enough to produce a stress intensity factor that was above the long crack threshold intensity factor of $\Delta K_{th} = 9{\cdot}4$ MPa $m^{1/2}$ for the given crack size. Even though the LEFM calculations indicated that the initial discontinuities would not lead to specimen failure, if they were treated as long cracks, evaluation of the fracture surface indicated that the near surface porosity did indeed contribute to the failure. Since small crack growth can occur below this ΔK_{th}, an explanation for this disagreement lies in looking at small crack growth.

Small crack growth is greatly influenced by the microstructure of the component and is often very unpredictable. It can be approximated by the extrapolation of the Paris equation into the small crack growth behaviour 'regime' as was done here. However, this extrapolation may have contributed to unrealistic calculations. Another source of error is the use of fatigue crack growth properties that were not measured for the microporosity specimens. It was hoped that the sound material constants A and n used in equation (9) could be used in the material with microporosity. However, it appears now that, compared to sound material, material with microporosity will likely have a lower threshold value and a faster crack growth rate at a given ΔK as a result of stress concentrations created around microvoids within the material. Shorter LEFM calculated specimen lives will result from either shifting the Paris equation up by increasing the constant A, or from increasing the slope of the equation by raising the value of the exponent n. Both would lead to shorter calculated specimen life.

Fatigue life calculations for macroporosity

Macroporosity fatigue life calculations by strain–life approach

An appropriate notch model must be selected to calculate the fatigue life of the macroporosity specimens using the strain–life approach. Both size and shape for the notch responsible for the failure must be defined for the notch. Since it was not possible in the present study to identify particular notches responsible for failures of the macroporosity specimens, the course of action taken was to perform test calculations using a variety of available notch models using notch (pore) size and shape data determined from microscopy.

As an initial step, specimen C4 was determined to be a representative specimen for the purpose of applying strain–life calculations. In specimen C4, the macroporosity was encapsulated at the specimen centre and did not extend as near the surface as it did in some specimens. Specimen C4 had three large macropores on the ground-back fracture surface. Based on the average dimension of the pores in C4, a spherical notch of radius 0·75 mm was selected as the representative notch. The cross-sectional area of this notch was close to the average pore area in specimen C4. Using the spherical notch model[21] for this size of notch gave agreement between calculated and measured fatigue life for specimen C4. In the current work, these stress concentration factors were determined from best fit lines to the curves found in the handbook of stress concentration factors by Peterson.[21] These assume the notch to be internal in an infinite body and so the surface stress concentration factor K_t was increased by 7% as mentioned earlier.

As a next step, results of the life calculations are compared with experimental lives in Fig. 20 using this 'representative' 0·75 mm radius notch for all specimens. Note that the data point for specimen C4 is

Table 7 Results of modelling single 200 μm diameter pore as surface crack

S_{max}, MPa	% of net section yielding	Experimental N_f, cycles	a_f, mm	Calculated N_f, cycles
862	79·2	153 and 381	1·57	27 400
790	72·6	3800	1·80	35 700
698	64·2	650 and 3476	2·07	51 900
395	36·3	19 299	3·04	291 000†
296	27·2	62 112	3·42	699 000†
198	18·2	517 015 and 52 858	3·81	2 360 000†
158	14·5	951 965	3·98	4 680 000†
126	11·6	Run-out* and run-out	4·15	Run-out†

Note: fatigue lives for runs at repeated stress levels are separated by 'and'.
*Run-out is 5×10^6 cycles.
†Small crack growth assumption was needed to make life predictions.

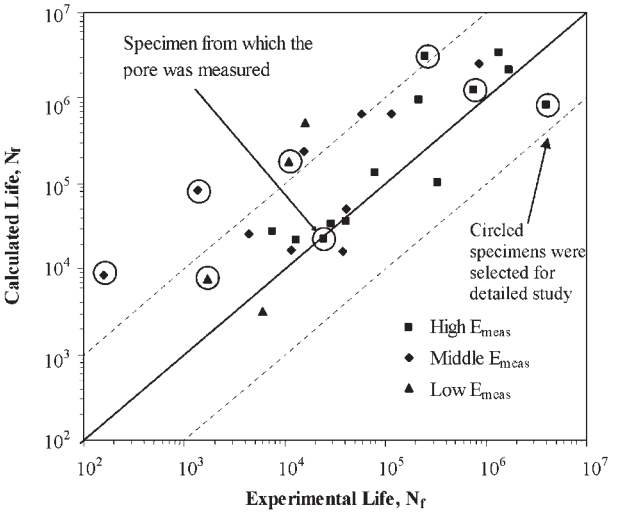

20 Calculated versus experimental life for strain–life modelling based on typical macropore sphere found in specimen C4; $R_{pore}=0{\cdot}75$ mm

indicated in the figure. Since an identical notch size is used in all specimens, the variables reflecting the different amounts of porosity in each specimen are E_{meas} and S_{calc}. Macropores cause a substantial loss of cross-sectional area within the specimen, and hence a large increase in the applied stress. Considering this, the calculated stress from equation (3) was used as the stress amplitude in the strain–life modelling. Agreement between experiment and calculation is good for about two-thirds of the specimens in Fig. 20, and poor for the other third. Also, where there is poor agreement, it is unfortunately non-conservative.

Eight specimens (circled in Fig. 20), four of which are above the upper $10\times$ life interval line, were selected for further analysis to see if using more scrutiny in the selection of the notch model, and the notch dimensions, would produce better agreement. These eight specimens are the same specimens listed in Table 4. Note that these eight specimens were tested over a range of stress amplitude levels. Specimens C10 and E6 were chosen for detailed analysis specifically for their unusually long and short lives, respectively. Each macroporosity casting group was represented in the eight selected specimens.

Aside from the 0·75 mm radius spherical notch model used in Fig. 20, hemispherical or 3-D ellipsoidal notches (the Sadowsky/Sternberg or the Neuber notch models) were used to model the stress concentration factors. The Sadowsky/Sternberg type notch was used for pores that loosely resembled the shape of a cigar or American football. Pores of this type required measurements of the major and minor axes, which were determined by microscopy of the 2-D polished surface images. The Neuber notch model was used for pores that were more disc-shaped. The plane of the ellipse is parallel to the loading direction for the Neuber notch with the axis of revolution about the minor axis. Notch size and shape data are required to develop a 'model' notch within the material, and this was determined from microscopy. Using these notch models, the stress concentration factors K_t ranged from 2·27 to 2·97. From K_t, a fatigue notch factor was calculated using equations (5) and (6). Table 4 contains the ellipsoidal notch information used in the specimens selected for analysis: notch type, major and minor ellipse axes length, K_t and K_f. In cases where a specimen contained multiple pores, the notch was created to fit the dimensions of the largest pore on the ground surface of the specimen.

Using S_{calc} from equation (3), the nominal strain ranges were determined from equation (1), and the notch root strain was determined from equations (7) and (8). The specimen life was calculated using equation (2), with the results shown in Table 8. Calculated versus experimental fatigue lives are shown in Fig. 21 using solid data points for strain–life modelling. Generally, the calculations are still non-conservative. The effectiveness of the local strain–life model with ellipsoidal notches in calculation of the fatigue life of specimens with macroporosity varied significantly. Unfortunately, no remarkable differences were observed during microscopy examination between the specimens that were in good and in poor agreement with the notch modelling.

However, there are fundamental factors that contribute to the modelling uncertainties and may be sources of disagreement between the notch calculations and tests: complex pore shape, an inability to determine a specific pore responsible for failure, the presence of multiple pores in the specimens, the use of infinite body notch models, use of bulk material properties of the microporosity specimens, and the use of a calculated stress based on the modulus E_{meas}. The shape of the porosity was very torturous and made the process of fitting a notch to the pore geometry difficult and not entirely quantitative. This contributes to uncertainty in the notch dimensions. Though many macropores were evident throughout the ground surfaces of some of the specimens, the fatigue life calculation only takes

Table 8 Results of modelling macropores as ellipsoidal notches using local-strain model

Specimen	Stress amplitude, S_a, MPa	Calculated stress, S_{calc}, MPa	Young's Modulus, E, GPa	Experimental N_f, cycles	Calculated N_f, cycles
H2	66	86	151	769 074	834 000
G7	53	73	143	249 752	Run-out*
C4	126	174	143	24 320	24 500
C10	66	92	141	4 053 800	295 000
C2	96	138	137	1365	60 275
E6	126	207	120	160	6800
E1	96	211	90	1935	4333
D5	53	120	87	10 812	124 000

*Run-out is 5×10^6 cycles or greater.

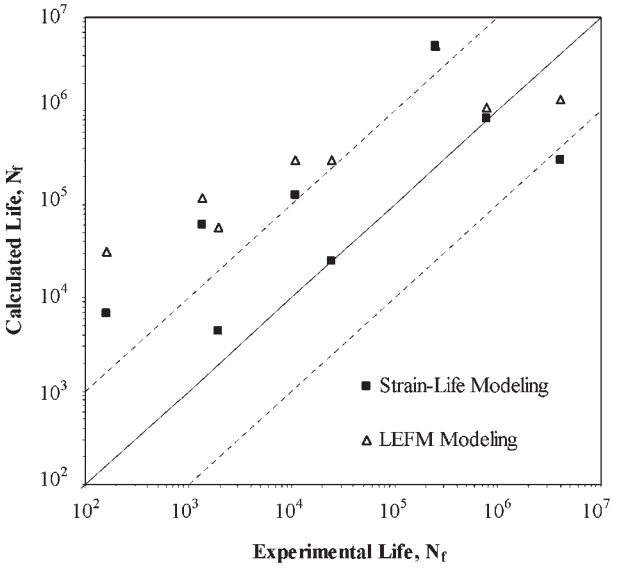

21 Calculated versus experimental life for strain–life and LEFM modelling for eight identified points in Fig. 20 using pore measurements given in Table 4

into account the influence of a single pore, or tightly spaced group of pores modelled as a single ellipsoidal notch. Strain–life material properties from the specimens with microporosity were used in the fatigue life calculations for the specimens with macroporosity. These material properties used are given in Table 2. This is believed to be an accurate representation of the specimens with macroporosity because the 'sound' portions of the specimens were observed to contain micropores ranging from approximately 10 to 200 μm in diameter. Essentially, the macropore notches reside within material having properties of the specimens with microporosity. Recall that the notch models assume an infinite body. However, as is evident in Figs. 16 and 17, the macropores are of a size comparable to the nominal area of the specimen. Therefore another shortcoming of the calculations is that the 'corrected' infinite body solution does not accurately reflect the true K_t of these specimens. The pores were also very large in relation to the overall dimension of the specimens. It may have been beneficial to use larger specimens or create specimens with smaller amounts of porosity. Either case would address these issues, and reduce the difference between the specimens and the notch model. Finally, to develop a truly predictive model, the stress input for the life calculation equations must be model-based, instead of using a measured stress S_{calc}.

Modelling macropores by LEFM approach

Modelling the fatigue lives of the eight selected specimens listed in Table 4 by LEFM was also performed. Since it could not be determined through fractographic analysis which pores were responsible for the failure of a particular specimen, the square root of the total surface area of the porosity was used to determine the initial crack length for each specimen as measured. It was anticipated that this approach would give a conservative estimate and would be applicable for life calculations. The crack length at fracture was determined to be the point of net section yielding and was determined in the same manner as a_f was found in the micropore LEFM calculations. The value of ΔK was determined using equations (10), (12) and (13) and the maximum nominal stresses encountered during testing. The Forman crack front model, equations (12) and (13), was again used as a result of the presence of surface porosity on all of the evaluated specimens, though actual crack nucleation regions could not be determined. The life calculation was made by numerically integrating equation (11), with the results shown in Table 9.

Fatigue lives calculated using LEFM are plotted in Fig. 21 versus experimental fatigue lives using 'open' symbols. The LEFM life calculations produced results that were generally in less agreement with the measurements than the notched strain–life calculations. Only one of the LEFM life calculations was conservative, with five specimens having calculated lives more than 10 times longer than what was observed experimentally. The initial crack length was taken as the square root of the total pore surface area found on the ground surface instead of just a single pore or group of pores that were thought to be responsible for the failure of the specimen, which should have led to conservative results. As with modelling the micropores, the use of crack growth properties taken from sound (keel block) material may have adversely affected the life calculations of the specimens with macroporosity. In summary, assumptions that may have resulted in disagreement between the model calculations and test data are: modelling macropores as the square root of the total pore area, uncertainty in the actual macropore sizes responsible for failure, and the lack of good crack front propagation models for material surrounding the macroscopic pore.

Table 9 Results of modelling macropores as crack

Specimen	S_{max}, MPa	Experimental N_f, cycles	a_i, mm	a_f, mm	Calculated N_f, cycles
H2	66	769 074	1·70	4·44	1 080 000†
G7	53	249 752	0·66	4·52	Run-out*†
C4	126	24 320	1·44	4·13	294 000
C10	66	4053 800	1·63	4·44	1320 000†
C2	96	1365	2·14	4·28	119 000
E6	126	160	2·33	4·13	31 400
E1	96	1935	2·41	4·28	56 400
D5	53	10 819	2·46	4·52	298 000†

*Run-out is 5×10^6 cycles or greater.
†Stress intensity factor threshold value was not exceeded.

Discussion

Cyclic and fatigue material properties were measured through strain and load controlled $R=-1$ testing of the microporosity specimens. Microporosity specimens had low $\Delta\varepsilon_p/2$ at high strain amplitudes and virtually no $\Delta\varepsilon_p/2$ at strain amplitudes lower than $\Delta\varepsilon/2=0{\cdot}006$. The fatigue limit S_f was also much lower than sound cast material. The difference in material properties was as a result of the occurrence of microporosity. Comparison of the micropore cast steel material with sound specimen properties revealed similar monotonic strengths, but reduced ductility. Percent reduction in area was significantly reduced by approximately a factor of 4, and though a direct comparison between per cent elongation was not possible, a value of 2·5% would be considered very low for cast steels of similar strength which normally have a per cent elongation near 20%. Microporosity had a significant influence on the cyclic and fatigue properties of the specimens with microporosity. The reduced ductility of the steel gave a lack of plastic strain observed during cycling, causing the elastic strain amplitudes to remain larger than the plastic strain amplitudes at all strain levels tested. This would cause the material to behave in a more brittle manner with increased crack growth rates and consequently reduced fatigue strengths at all strain amplitudes. Evidence of this is shown in the reduced fatigue limit at 5×10^6 cycles which is less than half of the S_f observed in the sound specimens. Further, the micropores themselves would act as stress risers within the specimen, further decreasing the crack nucleation times.

Specimens containing macroporosity performed significantly more poorly than specimens that contained microporosity in fatigue testing. For a stress amplitude of 126 MPa, the two specimens with microporosity resulted in run-out tests; their fatigue lives were greater than 5×10^6 cycles. At the same stress level, eight macroporosity specimens in all three groups were tested, and the lives of these specimens ranged from 160 to 41 000 cycles. Within the three macroporosity specimen groups, the 'least' and 'middle' porosity groups were found to have similar fatigue lives and both outperformed the 'most' porosity group. A correlation between the measured specimen modulus E_{meas} the porosity level (represented by specimen group), and the specimen fatigue life was observed. The specimen modulus E_{meas} was shown to have a strong correlation with the fatigue life of the specimens and was subsequently used as a new way of grouping the specimens. Generally, specimens with higher E_{meas} outperformed the lower modulus specimens, but significant scatter could still be observed within the modulus groups, particularly noticeable in the modulus 110–139 GPa grouping, as well as in the calculated stress grouping. E_{meas} appears to be a better indicator of fatigue performance than specimen grouping, but this information alone cannot be accurately correlated to the life of a specimen.

The most common pore size found on the polished microporosity specimen surfaces with microporosity was approximately 8 μm in diameter. However, sizes up to 20 μm in diameter were also observed. Larger pores, on the order of 200 μm in diameter, were observed on several of the specimen fracture surfaces. Though these larger pores may not be numerous within the current material, they have a significant influence on the fatigue life. From local strain–life modelling, a notch diameter of 200 μm gave good agreement with fatigue testing. LEFM modelling of micropores did not produce accurate life calculations as a result of the small crack growth behaviour of the micropores and lack of crack growth property data.

As a result of the small size of the micropores, the extent of microporosity could not be determined conclusively, neither by examination of the radiographs nor through the examination of the fracture surfaces. Information on the size and distribution of microporosity was gathered through microscopy conducted on ground surfaces of the microporosity specimens. The total microporosity area was determined to be 0·65% or less within the microporosity specimens. This relatively small percentage of microporosity caused significant reduction in ductility performance, which concurs with a study by others who found that microporosity values greater than 0·5% significantly reduced per cent elongation and per cent reduction in area while having little effect on strength properties.[27]

For the macroporosity specimens, it was determined that strain–life calculations using a spherical notch radius of 0·75 mm gave agreement with the test data to within one decade for 20 out of the 27 of the specimens tested. The notch radius used in the calculations was chosen because it agrees with the pore radius observed via SEM in a 'typical' macroporosity specimen and the equivalent radius of porosity on ASTM standard radiographs.[17] The disagreement between the measured and calculated lives of the specimens with macroporosity was primarily non-conservative for both the strain–life and LEFM approaches, with LEFM giving more disagreement. The largest disagreement between the calculations and test data was observed at the lowest lived specimens (highest stress levels).

Modelling the effect of macroporosity using the strain–life and LEFM approach was hindered by the torturous shape of the shrinkage porosity and the large size of the macropores relative to the specimen diameter. Determining a proper value for K_t was difficult. The complex shape of the porosity is not the idealized hemispherical and three-dimensional elliptical notches. Here, as in other investigations, an envelope was constructed around the pore to approximate it as a 200 μm sphere (in the case of microporosity), and a 0·75 mm dia. sphere and three-dimensional notches as shown in Table 4 (in the case of macroporosity).[9,10] This is the first attempt by these authors to relate the fatigue life to the size of the porosity as it may be found on an X-ray or a cut section. The crack initiation and growth from pores is much more complex than this and is influenced by the detailed geometry of pores deep in the solidified structure with smaller radii and sharper corners. However, crack initiation and growth from pores also depend upon location of these pore features relative to the grain boundaries and the orientation of grain boundaries on the pore periphery relative to the

stress.[28] These issues may be difficult to include in a general predictive model, and a more thorough analysis that takes into account more details of pore shape and other issues will have to be done in the future to see if predictions can be improved. Modelling the effect of macroporosity using LEFM was hindered by using crack growth properties taken from sound 'keel' block material, as well as the large size of macroporosity located within the specimens, which is expected to increase the stress amplitude in the section. Examination of the porous material fracture surfaces with the SEM showed that many specimens had no clear indication of crack nucleation, FCG, or final fracture regions on either the micro- or macroscopic levels. However, several specimens tested did have FCG and final fracture regions similar to the micropore material low strain amplitude specimens on both the micro- and macroscopic levels, but there was no clear indication of crack nucleation.

Summary and conclusions

Cast steel containing a variation in porosity from micro- to macro- levels was tested for monotonic strength and fatigue, and the experimental fatigue results were then compared with fatigue calculation models. No porosity was seen in radiographs of the specimens with microporosity, whereas the 'least' and 'middle' macroporosity groups appeared to contain similar amounts of porosity, and the 'most' macroporosity group contained noticeably greater porosity.

Based on the preliminary calculations performed here, there is evidence that using strain–life models for cast steel with microporosity can provide an engineering approach sought to couple casting simulation prediction of porosity with the prediction of part fatigue performance. Since microporosity in steel is not usually detected by radiography (or other nondestructive inspection techniques), the possibility of its presence in parts can be considered in the design process either by 'what-if' analysis, or by integrating casting process simulations with the design analyses. When the fatigue test results for both the micro- and macroporosity specimens are compared with sound keel block data, the full range of mechanical property degradation caused by porosity is seen. The issues which are believed to prevent good agreement between calculations and test specimen life data for the macroscopic specimens continue to be investigated.

Acknowledgements

This research was undertaken as part of the Integrated Design of Steel Castings for Service Performance project which is funded by the United States Department of Defense through the American Metalcasting Consortium (AMC) PRO-ACT program. AMC's PRO-ACT programme is sponsored by Defense Supply Center Philadelphia (DSC, Philadelphia, PA, USA) and the Defense Logistics Agency (DLA, Ft. Belvoir, VA, USA). This research is also conducted under the auspices of the Steel Founders' Society of America, and through substantial in-kind support, guidance and interest from SFSA member foundries. In particular, the authors would like to thank Harrison Steel for several trial iterations on the casting of test specimens and the final test specimen castings, Alloy Weld Inspection Co. for their digital and film radiography of the fatigue test specimens, and MAGMA GmbH for their support of the porosity prediction model used to design the test specimen castings.

References

1. ASTM: in '2002 Annual book of ASTM standards', Vol. 03.03, 189–191; 2002, West Conshohocken, PA, American Society of Testing and Materials.
2. ASTM: in '2002 Annual book of ASTM standards', Vol. 03.03, 81–83; 2002, West Conshohocken, PA, American Society of Testing and Materials.
3. ASTM: in '2002 Annual book of ASTM standards', Vol. 03.03, 125–127; 2002, West Conshohocken, PA, American Society of Testing and Materials.
4. M. KOHNO and M. MAKIOKA: *AFS Trans.*, 1970, 9–16.
5. K. CHIJIWA, T. NAKAYAMA and M. IMAMURA: *CIF*, **36**, 1–12.
6. J. G. CONLEY, B. MORAN and J. GRAY: 'Aluminum in automotive applications', Vol. 1350, 25–38; 1998, SAE Special Publications.
7. Q. G. WANG, D. APELIAN and D. A. LADOS: *J. Light Metals*, 2001, **1**, 73–84.
8. C. M. SONSINO and J. ZIESE: *Int. J. Fatigue*, 1993, **15**, 75–84.
9. P. HEULER, C. BERGER and J. MOTZ: *Fatigue Fract. Eng. Mater. Struct.*, 1992, **16**, 115–136.
10. S. JAYET-GENDROT, P. GILLES and C. MIGNE: 'Fatigue and fracture, Vol. 1', Vol. 350, 107–116; 1997, American Society of Mechanical Engineers, Pressure Vessels and Piping Division.
11. T. MANSSON and F. NILSSON: *Int. J. Cast Met. Res.*, 2001, **13**, 373–378.
12. P. HAUSILD, C. BERDIN, P. BOMPARD and N. VERDIERE: *Mater. Sci. Eng. A*, 2002, **335**, 164–174.
13. R. HARDIN and C. BECKERMANN: in '2002 SFSA technical and operating conference proceedings', Chicago, IL, Steel Founders' Society of America, Paper 4.5, 1–10.
14. K. D. CARLSON, Z. LIN, R. A. HARDIN, C. BECKERMANN, G. MAZURKEVICH and M. C. SCHNEIDER: Proc. Conf. on 'Modeling of casting, welding and advanced solidification processes X', Destin, Florida, May 2003, 295–302.
15. R. I. STEPHENS: 'Fatigue and fracture toughness of five carbon or low alloy cast steels at room or low climatic temperatures', Carbon and Low Alloy Technical Research Committee, Steel Founders' Society of America, Des Plaines, IL, 1982.
16. ASTM: in '2002 Annual book of ASTM standards', Vol. 03.01, 569–583; 2002, West Conshohocken, PA, American Society of Testing and Materials.
17. K. CARLSON, S. OU, R. HARDIN and C. BECKERMANN: *Int. J. Cast Met. Res.*, 2001, **14**, 169–183.
18. ASTM: in '2002 Annual book of ASTM standards', Vol. 03.01, 738–745; 2002, West Conshohocken, PA, American Society of Testing and Materials.
19. ASTM: in '2002 Annual book of ASTM standards', Vol. 03.01, 60–81; 2002, West Conshohocken, PA, American Society of Testing and Materials.
20. C. R. BROOKS and A. CHOUDHURY: 'Failure analysis of engineering materials'; 2002, New York, McGraw-Hill.
21. R. E. PETERSON: 'Stress concentration factors'; 1974, New York, Wiley-Interscience.
22. EUBANKSR. A.: *Trans. ASME*, **76**, Appl. Mech. Section, 57–62.
23. R. I. STEPHENS, A. FATEMI, R. R. STEPHENS and H. O. FUCHS: 'Metal fatigue in engineering', 2nd edn; 2000, New York, Wiley-Interscience.
24. Society of Automotive Engineers: 'Fatigue design handbook', Vol. 4, 29; 1968, Warrendale, PA, SAE.
25. R. G. FORMAN and V. SHIVAKUMAR: 'Fracture mechanics', 17th volume, ASTM STP 905, Philadelphia, ASTM, 1986, 59–74.
26. ASTM: in '2002 Annual book of ASTM standards', Vol. 03·01, 603–644; 2002, West Conshohocken, PA, American Society of Testing and Materials.
27. J. A. GRIFFIN, R. D. GRIFFIN and C. D. PEARS: in '2000 SFSA technical and operating conference proceedings', Chicago, IL, Steel Founders' Society of America, Paper 2.5, 1–10.
28. J.-Y. BUFFIÈRE, S. SAVELLI, P. H. JOUNEAU, E. MAIRE and R. FOUGÈRES: *Mater. Sci. Eng. A*, 2001, **316**, 115–126.